POLITECNICO DI TORINO
Repository ISTITUZIONALE

Evaporation in action sensed by multiwavelength Doppler radars

Original
Evaporation in action sensed by multiwavelength Doppler radars / Tridon, F., Battaglia, A., Watters, D.. - In: JOURNAL OF GEOPHYSICAL RESEARCH. ATMOSPHERES. - ISSN 2169-897X. - 122:17(2017), pp. 9379-9390. [10.1002/2016JD025998]

Availability:
This version is available at: 11583/2807112 since: 2020-03-29T17:16:42Z

Publisher:
Blackwell Publishing Ltd

Published
DOI:10.1002/2016JD025998

Terms of use:

This article is made available under terms and conditions as specified in the corresponding bibliographic description in the repository

Publisher copyright

(Article begins on next page)

08 September 2026

AGU PUBLICATIONS

JGR

Journal of Geophysical Research: Atmospheres

RESEARCH ARTICLE
10.1002/2016JD025998

Evaporation in action sensed by multiwavelength Doppler radars

Frédéric Tridon[1], **Alessandro Battaglia**[1,2], **and Daniel Watters**[1]

[1]Earth Observation Sciences, Department of Physics and Astronomy, University of Leicester, Leicester, UK, [2]National Center for Earth Observation, University of Leicester, Leicester, UK

Key Points:
- Dual-frequency radar retrieved profiles of drop size distribution feature the signatures of the evaporation process
- Under light rain conditions dominated by evaporation, the shrinking of raindrops diameter can be used as a signature of the ambient humidity
- Relative humidity profiles retrieved via the DSD profile and Raman lidar exhibit less than 10% difference

Correspondence to:
F. Tridon,
f.tridon@leicester.ac.uk

Citation:
Tridon, F., A. Battaglia, and D. Watters (2017), Evaporation in action sensed by multiwavelength Doppler radars, *J. Geophys. Res. Atmos.*, *122*, 9379–9390, doi:10.1002/2016JD025998.

Received 26 SEP 2016
Accepted 26 JUL 2017
Accepted article online 1 AUG 2017
Published online 7 SEP 2017

Abstract This work documents a rain case dominated by evaporation which occurred at the Atmospheric Radiation Measurement site in Oklahoma on 15 September 2011. A recently developed algorithm, applied to radar Doppler spectra measured at K_a and W band, provides the vertical evolution of binned drop size distributions (DSDs) and of the vertical wind. Such retrieved quantities are used in connection with relative humidity (RH) profiles to derive evaporation rates and atmospheric cooling rates. In addition, in regions of stationarity and of light rain, when other microphysical processes are negligible, the presented case study suggests the possibility of retrieving RH profiles from the vertical evolution of the drop size distributions. The key is to characterize the gradient of the rain mass flux between successive levels. Such signal is particularly weak and can be enhanced thanks to a substantial averaging of the retrieved DSD over approximately 5 min and 250 m (eight range gates). The derived profile agrees with the retrieval from coincident Raman lidar observations within a 10% RH difference. These results suggest that other rain microphysical processes could be studied by combining the radar-based DSD retrieval with ancillary RH observations.

1. Introduction

The understanding of the vertical evolution of rain drop size distribution (DSD) is critical for properly predicting rainfall at the ground from remote sensing measurements (e.g., in radar meteorology, for producing effective vertical profiling radar corrections) and also for understanding feedback mechanisms associated to the invigoration and the lifetime of precipitating systems. Unfortunately, even below cloud base, the vertical evolution of DSDs is the result of the complex interplay between different microphysical (coalescence, spontaneous and collisional breakup, differential sedimentation, and evaporation) and dynamical (up and downdraughts and advection) processes [e.g., *Brown*, 1993; *Hu and Srivastava*, 1995; *Beheng*, 2010].

Evaporation is the only warm subcloud microphysical process which involves a phase change (thus, a considerable energy exchange associated with the enthalpy of vaporization) and which induces a change in the total condensed liquid water content. Studies based on the isotopic composition of tropospheric water vapor [*Worden et al.*, 2007] have shown that, in the Tropics, rainfall evaporation can significantly contribute to the lower troposphere humidity and to the heat and moisture budgets of clouds, with typically 20% (and peaks of 50%) of rainfall evaporating near convective clouds. While several authors have specifically investigated evaporation from a theoretical point of view [*Srivastava*, 1987; *Li and Srivastava*, 2001; *Seifert*, 2008], observational studies have only focused on specific type of clouds (drizzling stratocumuli in particular) [e.g., *O'Connor et al.*, 2005; *Comstock et al.*, 2007] or very dry semiarid environments [*Rosenfeld and Mintz*, 1988]. More recently, attention has shifted toward the assessment of the effect of evaporation on retrieved water content and total drop concentration profiles [*Williams*, 2016] and polarimetric observables [*Kumjian and Ryzhkov*, 2010; *Xie et al.*, 2016] in order to improve hydrometeorological rainfall estimations.

This work capitalizes on a novel dual-frequency radar technique, which allows for rigorous retrieval of the vertical evolution of binned DSD and vertical velocities, and investigation of a case study where evaporation does represent the dominant rain microphysical process affecting the vertical evolution (section 2). This occurs only for fairly low rain rates. In this peculiar situation, comparisons with Raman lidar retrieval and radio sounding observations show that the knowledge of the vertical evolution of the DSD can be used to reconstruct the vertical profile of the relative humidity (RH). As will be discussed in section 3, the main motivation of this work is not to propose a new RH retrieval, which would be only applicable to a small number of light

©2017. The Authors.
This is an open access article under the terms of the Creative Commons Attribution License, which permits use, distribution and reproduction in any medium, provided the original work is properly cited.

rain cases, but to demonstrate that the DSD retrieval is sensible and can be used in more general cases to study other rain microphysical processes such as collision and breakup. In this regard, future work combining the radar retrieval with ancillary measurements of RH such as from the Raman lidar may enable the ability to disentangle the effect of evaporation from other microphysical processes.

2. Strong Evaporation Case Study

On 15 September 2011, a stationary front over the Rocky mountains associated with a cold and dry low-level air mass with northeasterly winds and a slowly lifting upper level trough moving from the southwest led to some widespread light rain over the Great Plains (a composite of surface weather, cloud cover, and radar reflectivity over the U.S. at 12:30 UTC can be found at http://www2.mmm.ucar.edu/imagearchive1/SatSfcComposite/20110915/sat_sfc_map_2011091520.gif). In particular, long-lasting stratiform rain was observed at the U.S. Department of Energy's Atmospheric Radiation Measurement (ARM) Program [*Ackerman and Stokes*, 2003] Southern Great Plains (SGP) Central Facility between 19:00 and 22:00 UTC (see Figure 1). Since various instruments are used in this study, it was decided to present all altitudes in kilometers above sea level (asl), the height of the ARM SGP being 320 m asl. In Figure 2, radio sounding observations at 17:44 (23:37) highlight the two air masses with fairly dry conditions below 1.5 km (1 km) asl and strong wind shear around 2 km (1.5 km) asl. Due to very dry low levels, most of the rain evaporated prior to reaching the surface, thus limiting the rain accumulation at the ground to low values (the gauges around the ARM Central Facility recorded between 0 and 1.5 mm rain accumulation).

The ARM (information about ARM instrumentation can be found in *Mather and Voyles* [2013], and references therein) K_a band Zenith-pointing Radar (KAZR), ceilometer, and Raman lidar observations (Figure 3) provide a general picture of the stratiform system with a two-layer cloud present in the late morning evolving into the precipitating system in the early afternoon (at about 19:00 UTC). The reflectivities (Figure 3a) and Doppler velocities (Figure 3b) help in the characterization of the vertical structure of the precipitating system with the ice phase reaching approximately 11 km and the melting level height (where the transition between solid and liquid precipitation is occurring as highlighted by the bright band in the radar reflectivity and the strong gradient in the Doppler velocity) initially at about 3.8 km asl and moving slightly downward during the first 2 h of precipitation. The ceilometer backscattering (Figure 3c) highlights the presence of a liquid cloud layer, which is known to produce strong backscattering and to rapidly attenuate the signal [*Hogan et al.*, 2003]; first, the cloud base moves down slowly from around 2.8 km asl in the morning then quickly moves 200–300 m upward after 19:30 UTC and disappears at around 20:00 UTC, about 1 h after the rain onset. These features are confirmed by the collocated Raman lidar backscatter measurements (which are not shown to avoid duplication) and strongly suggest the occurrence of collection of cloud droplets by the raindrops falling through the cloud layer. After 21:30 UTC, some cloud layers reappear intermittently at various levels while the rainfall intensity diminishes.

Within the rain layer and during the first phase of the rain event, the radar reflectivity and backscattering profiles are characterized by a moderate and strong increase with height, respectively. While these properties can be the signatures of diverse microphysical processes (e.g., drop breakup), they are consistent with evaporation occurring in a dry environment. Two radio soundings were available at the ARM site at 17:44 and 23:37 UTC, as marked in Figure 3a. High-resolution evolution of RH profiles can also be provided by Raman lidar observations [*Turner et al.*, 2002]. The ARM Raman lidar retrieval of RH vertical profiles [*Flynn and Sivaraman*, 1998, 1998] is shown in Figure 3d, with meaningful values up to the full extinction of the signal (i.e., 3 to 4 km asl). This ensemble of observations consistently confirms the presence of a very dry layer before the rain (black line in Figure 2) with 10–15% RH between 1.1 and 1.4 km asl and RH less than 50% below 1.6 km asl. During rain, the layer between 1.2 and 1.5 km asl clearly moistens with the RH exceeding 80% after 23:30 UTC (blue line in Figure 2). Since the ERA Interim reanalyses of the vertical integrated moisture flux divergence (not shown) suggests that there was no significant moisture advection over SGP during that period, such moistening can be plausibly caused by strong rain evaporation. The 17:44 radio sounding also captures the presence of the cloud layer detected by the lidar with 100% RH between 2.7 and 2.9 km asl.

2.1. Radar Retrieval of the DSD Evolution

Dual-frequency profiling radar observations are innovative and only available at very few locations in the world. Even at SGP, such observations are rare, in particular, because the W band Scanning ARM Cloud Radar

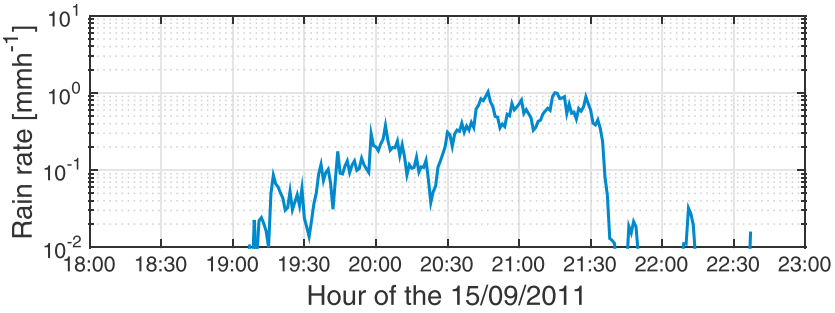

Figure 1. Rain rate observed by the 2DVD disdrometer at the ARM SGP central facility.

is operated only intermittently in vertically pointing mode. Thus, within this whole rain event, only four periods of 25 min are available for dual-frequency radar retrievals. Among these, one corresponds to significant rain rates (between 19:30 and 20:00 UTC; see Figure 1) and will be further analyzed.

Radar Doppler spectra represent the spectral reflectivity per bin of Doppler velocity. Thanks to the relationship between drop fall speeds and sizes, the shape of Doppler spectra obtained in a vertically pointing mode is intimately related to the particle size distribution, with the mean air motion displacing all hydrometeors equally and simply shifting the whole spectra along the Doppler velocity axis. On the contrary, depending on the position within the radar volume, the apparent velocity of similar-sized hydrometeors can be modified differently by air turbulence, wind shear, and/or cross wind, which results in the so-called spectral broadening. As a result, the retrieval of DSD from Doppler spectra relies on accurate estimates of spectral broadening and vertical air motion which are not realistically possible with a single-frequency Doppler spectrum.

To overcome this issue, *Tridon et al.* [2013] and *Tridon and Battaglia* [2015] have proposed a variational method (Optimal Estimation, OE) exploiting dual-Doppler spectra at K_a and W band to retrieve binned rain DSDs, vertical wind speed, and air broadening. The technique has been recently refined and extensively validated using a light precipitation event which occurred in Finland [*Tridon et al.*, 2017], the characteristics of which are very similar to the case study under examination. The retrieval is applied to KAZR data [*Matthews et al.*, 2011a] and WSCAR data [*Matthews et al.*, 2011b] in the region delimited by the black rectangle in Figure 3, between 19:32 and 19:57 UTC starting from the lowest available observations at W band (700 m above ground level, agl) up to 3.3 km asl in order to ensure that all particles are in the liquid phase. The radar observations are mapped onto a common time-height grid with resolution of 4 s and 30 m.

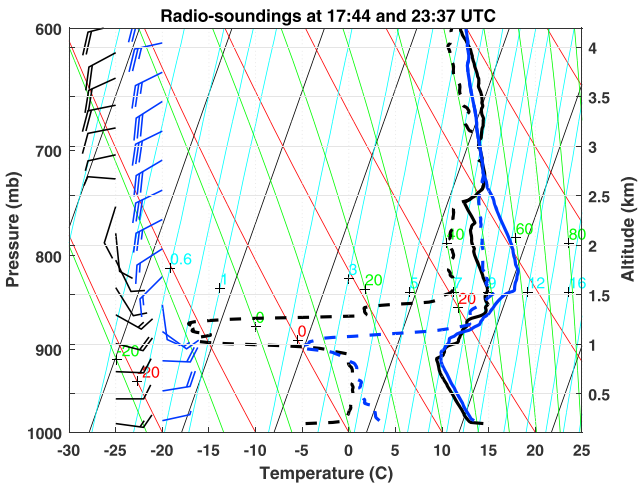

Figure 2. Atmospheric temperature (continuous lines) and dewpoint temperature (dashed lines) profiles for 17:44 (black lines) and 23:37 UTC (blue lines). The soundings are plotted in a skew T-log(p) diagram with constant mixing ratios (contour levels expressed in g kg^{-1}), dry and moist adiabats (contour levels expressed in °C) indicated with cyan, red, and green colors, respectively. Wind velocities and directions are indicated on the left-hand side of the plot for the two radio soundings with the same color coding. One long barb corresponds to 10 knots or 5.14 m/s.

As an example, the vertical evolutions of the K_a and W band Doppler spectra at 19:49:51 UTC are shown in Figures 4a and 4b, respectively. At large Doppler velocities (i.e., large diameters), the scattering differences at the two frequencies are made evident with Mie scattering notches around 6 m s^{-1} at W band. The retrieved vertical wind (positive downward) is indicated at each level by the black crosses. Another interesting feature is the peak observed by both radars at low Doppler velocities above 2.8 km. The position of this peak corresponds exactly to the vertical wind estimate,

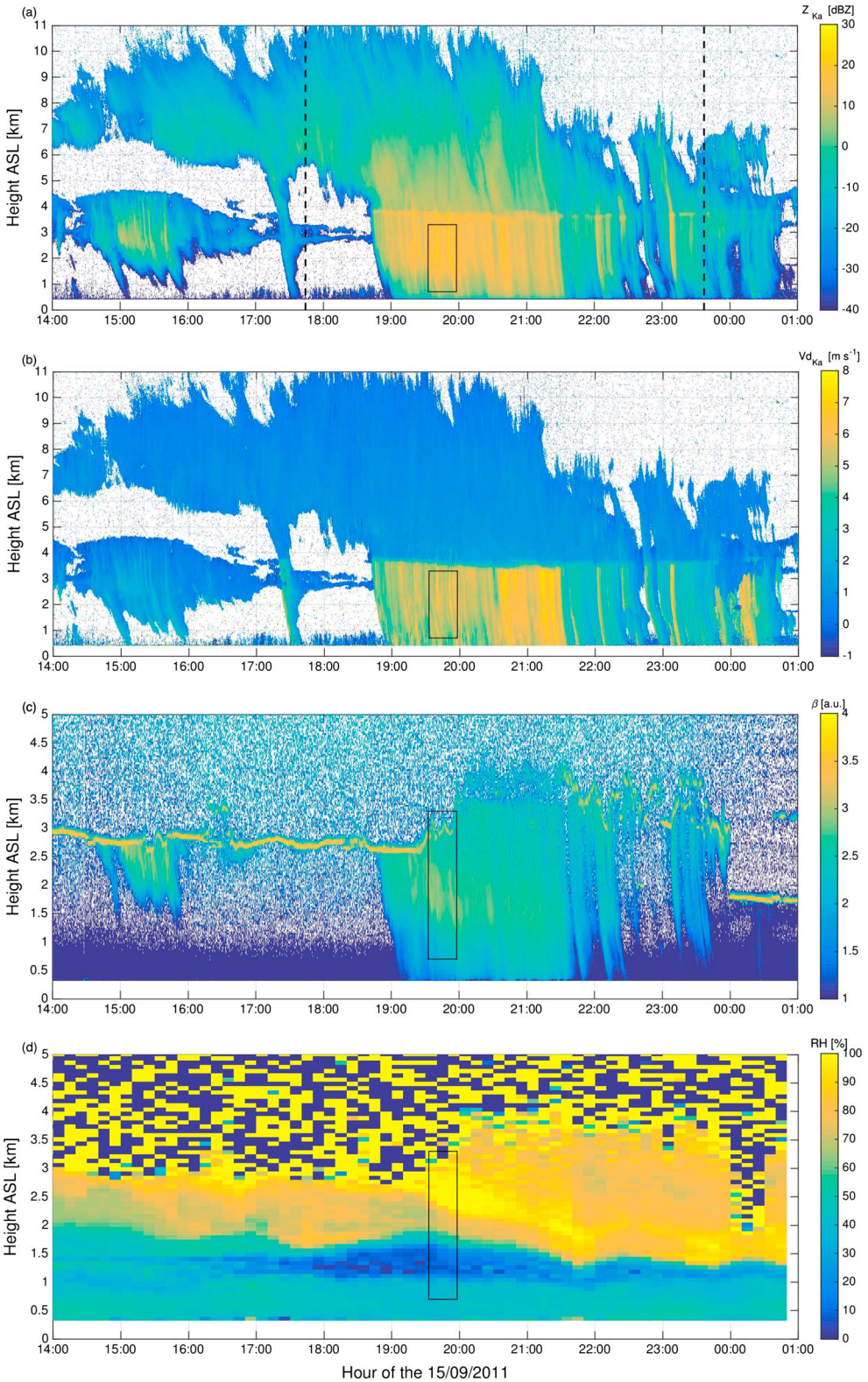

Figure 3. Time-height plots of the (a) KAZR reflectivity, (b) KAZR Doppler velocity, (c) ceilometer backscatter, and (d) Raman lidar relative humidity retrieval observed at the ARM SGP central facility on 15 September 2011, between 14:00 and 1:00 UTC. Within this period, two radio soundings were launched at the ARM facility at the times indicated by the black dashed lines in Figure 3a.

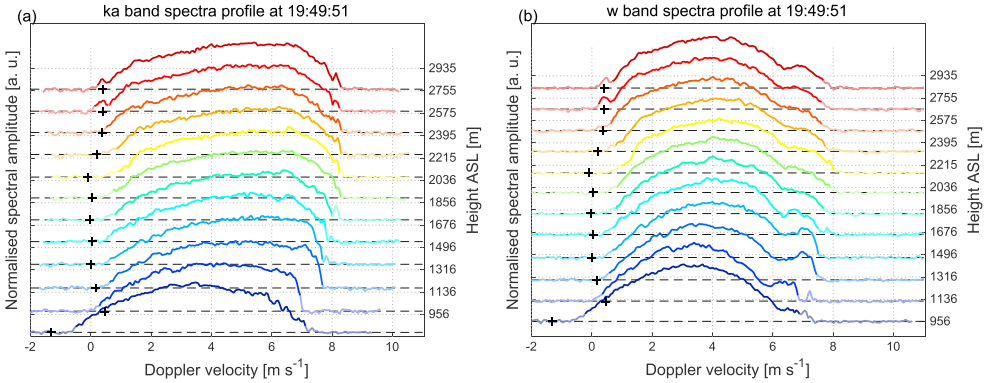

Figure 4. Doppler spectra for (a) K_a and (b) W band radars for few selected heights measured at 19:49:51 UTC. Bright colors indicate the good signal-to-noise portions of the spectra which are actually used in the retrieval of the DSD. The black crosses correspond to the vertical winds obtained within the framework of the DSD retrieval [*Tridon et al.*, 2017].

which suggests that it must be produced by droplets with a negligible velocity, thus confirming the presence of a cloud layer aloft.

The retrieval of the DSD makes use of the attenuation produced by rain at each layer and cannot separate the contribution from the cloud. Therefore, the retrieved DSDs averaged over 6 min are shown in Figure 5 up to the base of the cloud layer only. The error associated with the lowest and highest retrieved DSDs is shown as light colored shadings. Through a quadratic sum, it includes two types of error sources, namely, the mean retrieval error provided by the OE and the standard deviation of all individual DSDs within the 6 min periods, which can be interpreted as the error due to the nonstationarity of rain as observed by radars. Certainly, a reduction of the error through averaging is expected but this conservative approach is driven by the fact that the different retrieved DSDs are not independent and that the natural variability cannot be described by a stochastic process.

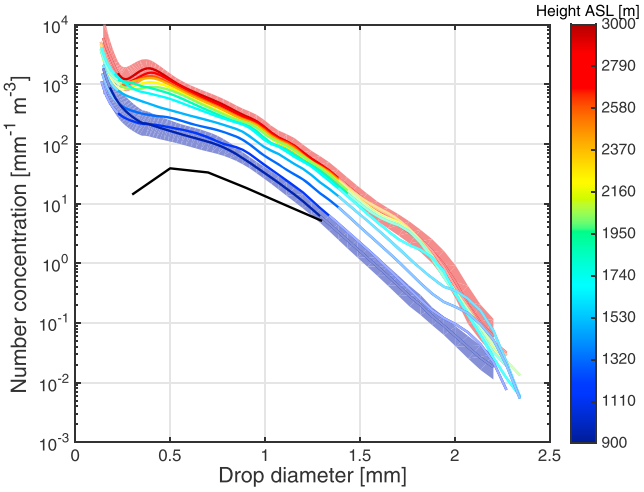

Figure 5. The 6 min averaged DSD vertical evolution before 19:49:51 UTC. The DSDs are retrieved according to the technique proposed by *Tridon and Battaglia* [2015] for the heights of the spectra shown in Figure 4. The black line shows the corresponding DSD measured by a collocated 2DVD disdrometer at the ground. Bright portions of the retrieved DSDs (roughly between 0.3 and 1.3 mm) indicate the diameter range which is contributing between 0.05 and 0.95% of the total evaporation rate. Blue and red shadings show the uncertainty of the retrieved concentration for the lowest and highest DSDs, respectively.

For drops larger than 0.3 mm, the shape of the retrieved DSDs is sensible and in agreement with the process of evaporation; this is specifically shown by a clear decrease in the concentration mainly between 1.8 and 1 km and preferentially for smaller drops as expected from theory [*Li and Srivastava*, 2001]. Without providing a full validation, the corresponding observations from the collocated disdrometer (2DVD) [*Kruger and Krajewski*, 2002] are consistent and confirm that evaporation is still active between the lowest radar retrieval and the ground, as it can be expected with a RH of 50% down to the ground (see Figure 3d). Because of the scarcity of large drops and of its small sampling volume, the disdrometer only detects raindrops with diameters smaller than 1.3 mm. Below 0.3 mm, the retrieved increase in concentration with decreasing size is associated with a rather large error. It is produced by very slight changes in the slope of the low velocity side of the Doppler spectra which can

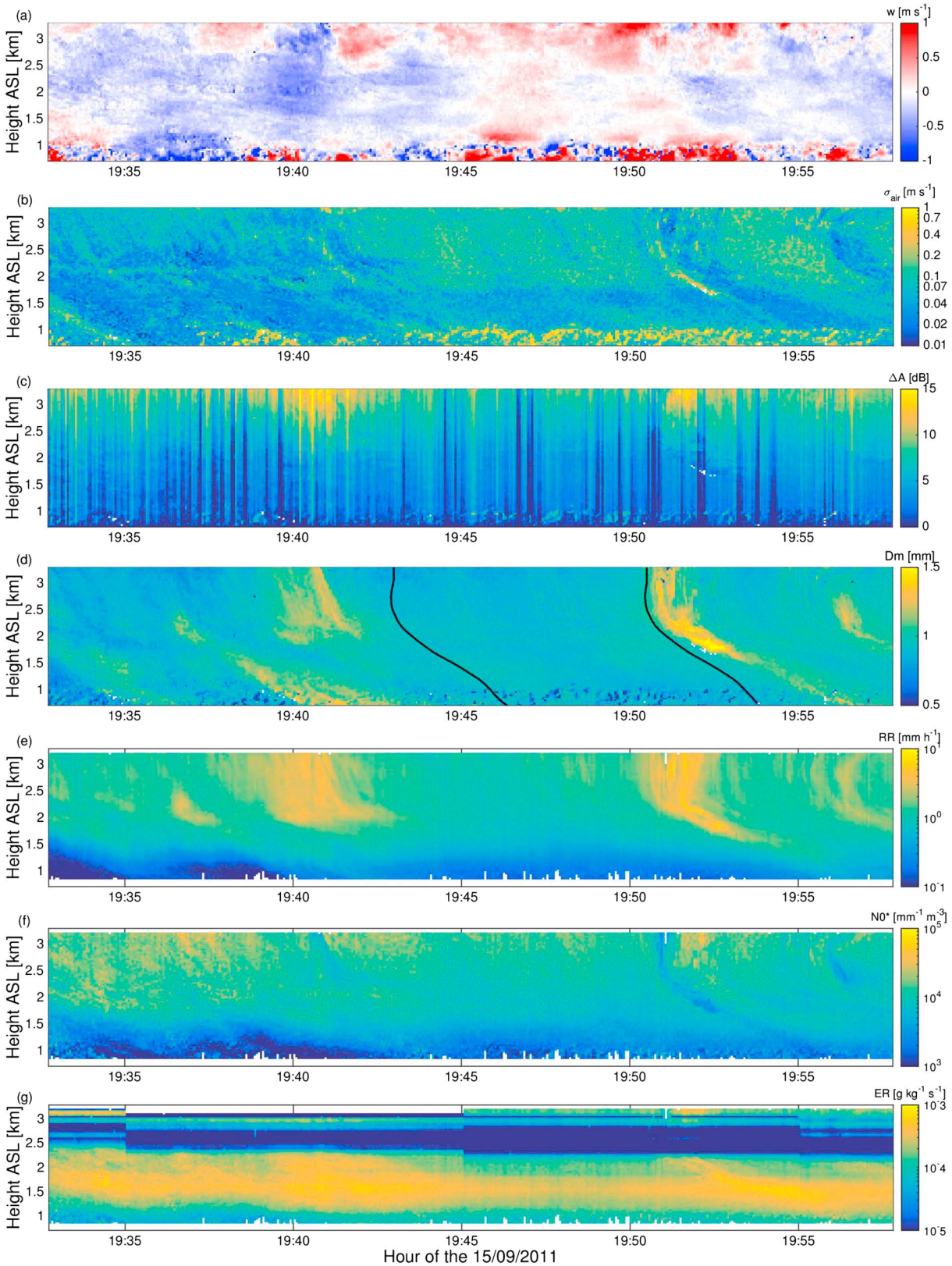

Figure 6. Time-height plots of radar retrieved quantities corresponding to the black square of Figure 3: (a) vertical wind, (b) air broadening, (c) differential attenuation, (d) mean mass diameter D_m, (e) rain rate RR, (f) normalized concentration parameter $N_0^\star$, and (g) evaporation rate. The period delimited by the black lines indicates a region where stationarity can be assumed.

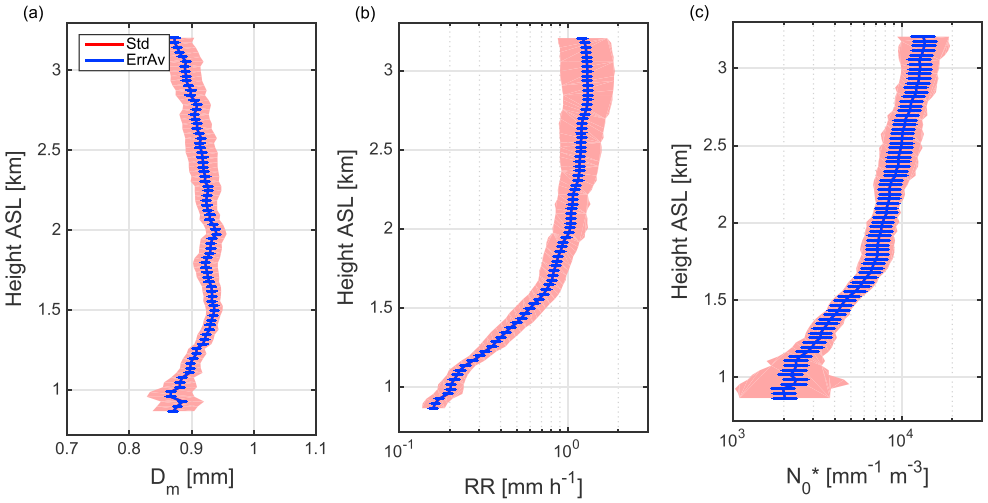

Figure 7. Mean vertical profiles of mean mass diameter D_m, rain rate RR, and concentration parameter $N_0^\star$ over the period shown in Figure 6d. Red shading and blue error bars show for each parameter the corresponding standard deviation and mean OE error over the same period, respectively.

be easily contaminated by noise. The fact that it is consistent with time and height suggests that it must have a physical explanation. It may be a sign that the fall velocity-diameter relation or the turbulence broadening model used in the retrieval [*Tridon and Battaglia*, 2015] is not adequate for such small drops. Despite their high concentration, these drops do not contribute much to the whole mass of water and their effect on the calculation of the evaporation rate is negligible (note that Figure 5 also highlights, for each DSD, the diameter range mainly contributing to the total evaporation rate as computed in section 2.3) and they do not affect the rest of this study. Therefore, the improvement of the retrieval at drops diameter lower than 0.3 mm will be the object of future work.

Some of the retrieval outputs for the whole period are shown in Figure 6. The vertical wind velocities (Figure 6a, positive upward) are always confined in the ± 1 m s^{-1} interval—as typical for stratiform precipitation—with the layer below 1 km exhibiting a large temporal variability, which is a signature of enhanced turbulence. This is confirmed by the air broadening (Figure 6b) which reaches maximum values at those levels. Air broadening is minimal in the other regions, thus signaling low turbulence conditions which are ideal for the applicability of the retrieval [*Tridon and Battaglia*, 2015]. Similarly, integrated two-way attenuations (Figure 6c) always exceed 4–5 dB, i.e., which has been found to be the threshold value for the applicability of the methodology [*Tridon et al.*, 2017]. Corresponding rain parameters, mean mass diameters D_m (Figure 6d), rain rate RR (Figure 6e), and concentration parameters $N_0^\star$ (Figure 6f) are derived from the retrieved DSDs and show the spatiotemporal variability of precipitation with the clear presence of several fall streaks. The one starting immediately after 19:50 UTC was previously analyzed in *Tridon et al.* [2013].

Between the fall streaks, the rain parameters are averaged over the apparent steady rain period (black lines in Figure 6d), providing an approximate description of the vertical profile of rain properties under these dry conditions (Figure 7). Within this selected period, the standard deviation of all individually retrieved parameters (nonstationarity error, red shading) generally dominates the mean retrieval error (blue error bars). In the remaining of this work, their quadratic sum will be taken as error for further calculations. Down to 1.5 asl, a slight increase of D_m toward the ground is somewhat visible (Figure 6a). Such behavior is expected under evaporation due to the preferential depletion of small drop size [*Kumjian and Ryzhkov*, 2010]. However, this is a weak signal and can be easily overcome by the behavior of few drops at the large end of the DSD (see Figure 5) as seems to be the case below 1.5 km. A much more obvious feature is the considerable reduction of rain rates and $N_0^\star$ (Figures 6a and 6c) when passing from 3 km to 1 km which can only be explained by evaporation. The plausibility of this assumption will now be verified with a simple evaporation model.

2.2. Evaporation Modeling

Evaporation of raindrops in a subsaturated environment is the result of a flux of water vapor from the raindrop's surface to the environment, which is driven by a positive gradient of vapor density between

the saturated raindrop surface and the drier environment. This water vapor flux is sustained by a conduction-driven heat flux through air from the environment to the cooler drop that heats the drop and allows the water molecules with sufficiently high kinetic energy to escape into the vapor phase. By equating these two terms the rate of change of raindrop diameter, D, can be computed by solving the differential equation [e.g., *Li and Srivastava*, 2001; *Kumjian and Ryzhkov*, 2010]

$$\frac{\mathrm{d}D}{\mathrm{d}t} = \frac{4}{D}\frac{(\mathrm{RH}/100) - 1}{F_K(v(D), T, p) + F_D(v(D), T, p)} \tag{1}$$

where F_K and F_D are terms related to heat conduction and vapor diffusion, respectively, and include the ventilation coefficients which are strongly dependent on the raindrop velocity $v(D)$ and slightly dependent on p and T via the kinematic and thermal diffusivity of air (full expressions can be found in *Rogers and Yau* [1989] and *Pruppacher and Klett* [1997]). RH is the ambient relative humidity ($0 < \mathrm{RH} < 100$ in subsaturated conditions).

By using the raindrops fall speed

$$v(D, z) = v_t(D, z) - w(z) \tag{2}$$

where v_t is the terminal fall speed corrected for air density (see equation (3) in *Tridon and Battaglia* [2015] which is based on *Atlas et al.* [1973] and *Frisch et al.* [1995]) and w is the vertical wind speed (defined positive upward), the differential equation (1) with respect to time can be converted into a differential equation with respect to height, z, measured downward from a given level

$$v(D, z)\, D\, \frac{\mathrm{d}D}{\mathrm{d}z} = 4\frac{(\mathrm{RH}/100) - 1}{F_K + F_D} \tag{3}$$

or equivalently

$$\frac{\mathrm{d}m(D, z)}{\mathrm{d}t} = v(D, z)\, \frac{\mathrm{d}m(D, z)}{\mathrm{d}z} = 2\pi\rho_L\, D\frac{(\mathrm{RH}/100) - 1}{F_K + F_D} \tag{4}$$

which provides the mass evaporation rate of the drop ($\rho_L = 10^3$ kg m^{-3} is the density of water).

If evaporation is the only mechanism controlling the evolution of the DSD (i.e., coalescence and breakup can be neglected), then by integrating equation (4) over all raindrops we get

$$\underbrace{\frac{\mathrm{d}F_m[v]}{\mathrm{d}z} + \frac{F_m[v_t]}{2H_\rho} + \frac{\mathrm{d}w}{\mathrm{d}z}\int_0^{D_{\max}} m(D)\, N(D)\, \mathrm{d}D}_{\text{Mass flux gradient term}} = \Big((\mathrm{RH}/100) - 1\Big)\underbrace{2\pi\rho_L \int_0^{D_{\max}} \frac{D\, N(D)}{F_K + F_D}\mathrm{d}D}_{\mathcal{I}} \tag{5}$$

where F_m is the mass flux computed using the velocity indicated in the square bracket. The second and third terms on the left-hand side come from the dependence of the fall speed on height and account for the fact that, due to the change of v_t and w, the mass flux is changing with height (i.e., it is decreasing when moving toward the surface because drop terminal fall speed decreases) even if no evaporation is present. The second term is derived based on the assumption that air density scales exponentially with a characteristic scale height H_ρ which is approximately equal to 8.4 km. It is important to stress that equation (5) is valid only in condition of stationarity (where the *DSD* is not changing with time).

2.3. Derivation of Evaporation and Cooling Rates

By dividing the right-hand side of equation (5) by ρ_{air} it is possible to compute the evaporation rate (in g kg^{-1} s^{-1}) at each level once the RH and the drop size distributions are known as

$$\mathrm{ER} = -\Big((\mathrm{RH}/100) - 1\Big)\frac{2\pi\rho_L \int_0^{D_{\max}} \frac{D\, N(D)}{F_K + F_D}\mathrm{d}D}{\rho_{\mathrm{air}}} = -\frac{\Big((\mathrm{RH}/100) - 1\Big)\mathcal{I}}{\rho_{\mathrm{air}}} \tag{6}$$

where the minus sign is introduced to make evaporation rates positive when $\mathrm{RH} < 100$. Results for the evaporation rates computed by using the RH profiles coming from the Raman lidar VAP are plotted in Figure 6g. There is obviously no evaporation in case of saturation (dark blue layer around 2.5 km asl), while maximum *ER* values reaching 0.5 mg kg^{-1} s^{-1} are found within the dry layer at about 1.5 km height.

The evaporation rate profile derived from the averaged DSD of Figure 5 is depicted as the black line in Figure 8. The uncertainty (grey shading) has contributions from the DSD error, and the Raman lidar retrieved RH error. The latter depends mainly on the water vapor mixing ratio and temperature profiles which are,

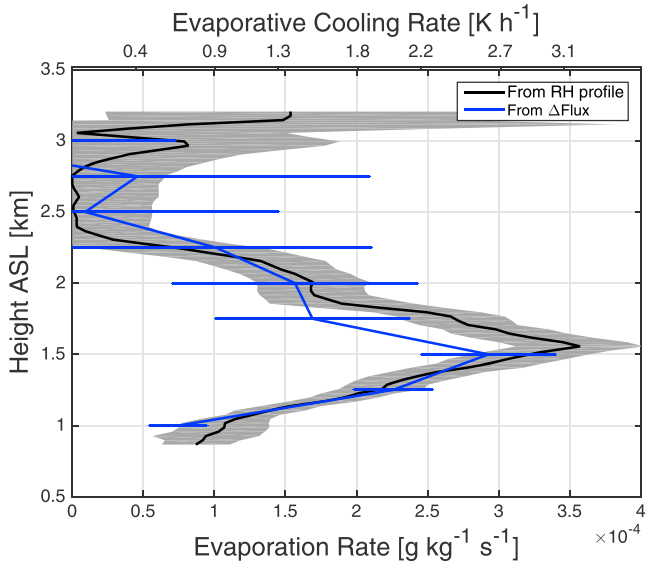

Figure 8. Vertical profile of the mean evaporation and cooling rates (bottom and top labels, respectively) for the fall streak bounded by the black lines in Figure 6d. The rates have been computed using the RH profile derived from the closest Raman lidar retrieval (black line) and from the mass flux gradient (blue line), respectively.

respectively, retrieved and used in the Raman lidar VAP. It has been estimated through the propagation of the water vapor mixing ratio error (available in the Raman lidar VAP) and using an error in temperature linearly increasing from 0.3 K at the surface to 2 K at 3 km agl (D. Turner, personal communication, 2017).

The evaporation rate derived from equation (6) can then be used to compute the feedbacks in the environment conditions caused by the evaporation process. The moistening equals the evaporation rate, whereas the environment cooling rate is simply given by

$$\frac{dT_{env}}{dt} = -ER\frac{L_{ev}}{c_p} \tag{7}$$

where L_{ev} is the latent heat of evaporation and c_p is the specific heat of dry air at constant pressure.

Using an accurate DSD profile, the vertical profile of the mean evaporation can also be directly deduced directly from the mass flux gradient (left term in equation (5)), i.e., without the need of any ancillary RH observation. The mass flux gradient is a particularly noisy signal at the resolution of radar observations, and a further 250 m averaging in range was deemed necessary to provide smooth variations with the mass flux gradient methodology.

Both methodologies are applied to the same averaged DSD of Figure 5 and compared in Figure 8. Overall, a reasonable agreement is obtained considering the uncertainties of both methodologies. They clearly show the dry layer (with peak of 0.3 mg kg^{-1} s^{-1} and 3 K h^{-1} for evaporation and cooling rates, respectively). Above 2.3 km, their behavior is not fully coherent. Negligible evaporation is obtained with the RH profile between 2.3 and 2.8 km because the Raman lidar VAP retrieval suggests saturation of this layer (see Figure 3d). However, this is questionable since the lidar and ceilometer are able to penetrate this layer up to an obvious cloud layer signature in the ceilometer backscatter at roughly 3 km asl (Figure 3c). In fact, the radar retrieval seems to better capture the height of this cloud layer with negative evaporation rates above 2.9 km. In the next section, these two estimates will be combined for the retrieval of RH profile. Inevitably, the difference between the evaporation rates profiles will result in difference between the Raman lidar and the retrieved RH profile.

2.4. Relative Humidity Retrieval

As shown in the previous section, the evaporation rate can be computed from both terms of equation (5). Then, if equation (5) holds, the RH can be retrieved at each level using

$$RH_{ret} = 100\left(1 + \frac{\frac{dF_m[v]}{dz} + \frac{F_m[v_t]}{2H_\rho} + \frac{dw}{dz}\int_0^{D_{max}} m(D)\,N(D)\,dD}{\mathcal{I}}\right) \tag{8}$$

For low rain rates, collisions between drops are scarce. However, the average distance between collisions depends considerably on the drop diameter. Over the analyzed domain, maximum retrieved drop diameters and rain rate are 3 mm and 5 mm h^{-1} (see Figure 6), respectively. According to *McFarquhar* [2004], the mean-free path (average distance between collisions of a drop with any other drop) of the largest drops in these conditions is of the order of 50 m, for a *Marshall and Palmer* [1948] distribution. Then, even if these drops have a very low concentration, collisions are probable and may modify the shape of the DSD between subsequent retrieval heights. To alleviate this issue, the focus will be made on a 6 min sample of the scene (between the two main fall streaks at 19:43 and 19:49 UTC; see black lines in Figure 6c) where the maximum retrieved drop diameters and rain rate are 2.5 mm (Figure 5) and 1.6 mm h^{-1} (Figure 6), respectively.

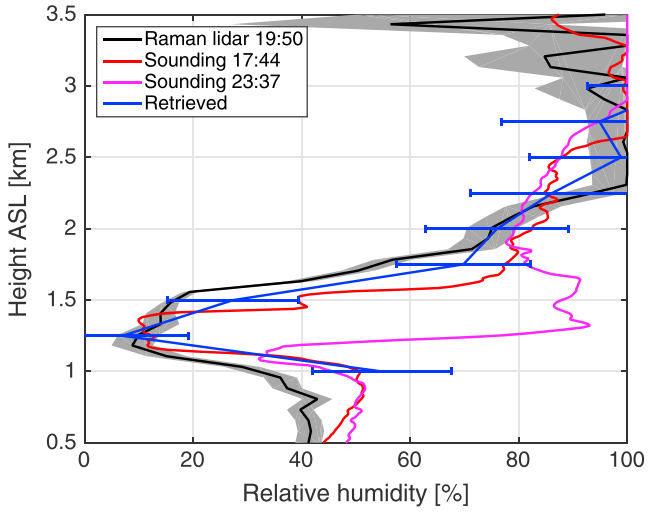

Figure 9. Vertical profiles of relative humidity. Red and magenta lines: derived from the radio soundings at 17:44 UTC and 23:37 UTC (plotted in Figure 2 as black and blue lines, respectively). Blue line with error bars: retrieved by using the DSDs averaged for the period highlighted by the black lines in Figure 6d (uncertainties are derived from the quadratic sum of the mean retrieval errors and the standard deviation of all individual DSDs over the 6 min period). Black line and grey shading: obtained from the ARM Raman lidar VAP.

Another potential difficulty arising when using the mass flux gradient is that the rain evolution as sampled by the radars is certainly not stationary, as, for instance, demonstrated by the presence of the fall streaks (note that this is not an issue when retrieving the evaporation rate from independent RH observations as in Figure 6g since no gradient is involved). Following *Hogan et al.* [2005] and *Kalesse et al.* [2016], this can be partially mitigated by simulating the slanted fall streaks in the radar time-height observation space. Such correction depends only on the hydrometeor fall speed and the horizontal wind profile. Ideally, coincident wind profiles observed by the collocated Doppler lidar should be used. However, such estimates are only available up to about 2 km agl. Therefore, observations from the closest radio sounding (17:44 UTC; see Figure 2) have been used in combination with fall velocities corresponding to the retrieved D_m to determine the fall streak of Figure 6d. As expected the low velocity between 3 and 2 km and the increasing velocity between 2 and 1 km lead to the two distinctive parts of the fall streak. The good visual agreement with the D_m structure suggests that the wind profile did not change much since the time of the radio sounding. Such correction is, however, approximative since it depends strongly on the drop fall speed and therefore on its diameter. Therefore, the nonstationarity of the rain can only be mitigated by time averaging. Two configurations are possible.

1. To average the DSDs over a period much longer than the fall streaks in order to cancel out their effects and then compute the mass flux gradient with such an averaged DSD. This option is unfortunately not applicable for the current case study because a longer averaging period would include the moderate rain fall streaks at 19:40 and 19:52 UTC for which collisions seem to have a significant contribution on the DSD vertical evolution.
2. To select a period within the event that features low rain rates and looks stationary at least for a time which corresponds to the typical fall time of the droplets through the depth used to compute the mass flux gradient. Since 250 m thick layers are considered for the mass flux gradient computation, 4 min is sufficient for droplets larger than 0.3 mm to pass through such layer. The period selected above fulfils this property (period between the black lines in Figure 6d).

Following the latter configuration, the retrieved RH is shown in Figure 9 (blue line), with all values within the range of possible physical values (i.e., between 0 and 100%) except above 2.8 km where the DSD retrieval is probably perturbed by the attenuation due to the cloud layer. Since the RH retrieval is based on the evaporation rate computed from the mass flux gradient, it has a resolution of 250 m. There is a good agreement with the Raman lidar retrieval at 19:50 UTC (black line) with a difference in RH of less than 10% overall. Above 2.3 km, the Raman lidar retrieval error becomes large due to low signal-to-noise ratio, and as described in the previous section, the retrieved saturation is questionable. With saturation retrieved at approximately 2.9 km, the radar retrieval seems to better capture the height of the cloud layer. Relative humidity observed by the radio soundings before and after the rain event is also shown in Figure 9 as red and magenta lines, respectively. Consistently with the radar and lidar retrievals (see also Figure 3d), they confirm the presence of a very dry layer between 1 and 1.5 km asl which get thinner over time while the rain evaporation moistens the ambient air.

Overall, the retrieved DSDs seem to provide a sensible description of the evaporation process and the shrinking of raindrops diameter when falling through this dry environment can be exploited as a signature

of the ambient humidity. The good agreement with the Raman lidar RH complements the validation of the DSD retrieval made in *Tridon et al.* [2017] with disdrometer observations. Furthermore, this suggests that the combination of the radar-based DSD retrieval with the Raman lidar-based RH retrieval will enable the opportunity to study other rain microphysical processes such as collision and breakup by independently taking evaporation into account. As a matter of fact, the retrieval of RH from DSD profiles as described in this paper cannot be widely applied because evaporation needs to be the dominant microphysical process. However, the main outcome of this work is that it paves the way toward the disentangling of rain microphysical processes from remote sensing observations. Such capability is potentially of great interest for the validation of the collision kernels and the self-collection and breakup parametrization which are used in bin and bulk microphysics models.

3. Conclusions

Evaporation processes crucially affect rain microphysics and storm dynamics. This study demonstrates that, for a stratiform case study characterized by strong evaporation, the profile of the raindrop size distributions (DSDs) retrieved by dual-frequency K_a-W band Doppler radars is consistent with independent observations of relative humidity. This result and the good performances in retrieving the DSDs at the ground [*Tridon et al.*, 2017] strongly suggest that such a technique allows for accurately profiling the evolution of the DSDs. In case of dry conditions, the knowledge of the vertical evolution of the DSD can be exploited in a twofold way.

1. To retrieve the evaporation and the cooling rates of the environment, if the relative humidity profile is known. These products can provide validation for microphysical modeling.
2. For the reconstruction of the relative humidity within the evaporating rain layer, under light rain conditions (i.e., when evaporation is the dominant microphysical process). In such instances, the evolution of the retrieved DSDs is exploited in conjunction with an evaporation model to retrieve the relative humidity profile. For the case study analyzed, the retrieved profile is in good agreement with the closest retrieval from a collocated Raman lidar. This can be indirectly seen as a demonstration of the quality of the dual-Doppler binned drop size distribution retrieval.

In future work, such observations of vertically pointing dual-Doppler radars should also be used with collocated polarimetric scanning radars (e.g., the ARM X Band Scanning ARM Precipitation Radar) in order to validate the vertical evolution of the polarimetric radar observables as predicted by the evaporation and collisional models [see, e.g., *Kumjian and Ryzhkov*, 2010; *Kumjian and Prat*, 2014] and, by so doing, to refine methodologies for estimating surface rain rates from radar measurements aloft in dry environments.

The good agreement between the DSD-retrieved RH profile and the Raman lidar RH in this evaporation-dominated case study suggests that their combination in a more general case should enable the opportunity to study other rain microphysical processes such as collision and breakup by independently taking into account evaporation. Therefore, though the retrieval of RH from DSD profiles as described in this paper cannot be widely applied, this work paves the way toward the exploitation of multisensor active remote sensing observations for disentangling rain microphysical processes. In this regard, future studies should explore the potential of radars in the G band, including the 183 GHz water vapor absorption line [*Battaglia et al.*, 2013; *Lebsock et al.*, 2015], in retrieving simultaneously liquid precipitation microphysics and water vapor profiles.

Acknowledgments
The authors thank F. Mercier and L. Barthes from LATMOS-IPSL for useful discussions and three anonymous reviewers for their helpful comments and propositions which greatly helped to improve the manuscript. They also express their gratitude to D. Turner for his recommendations regarding the use of ARM Raman lidar VAP retrieval. The work done by A. Battaglia and F. Tridon was funded by the project "Calibration and validation studies over the North Atlantic and UK for the Global Precipitation Mission" which was funded by the UK NERC (NE/L007169/1). This research used the SPECTRE and ALICE High-Performance Computing Facilities at the University of Leicester. Data were obtained from the U.S. DOE ARM Climate Research Facility http://www.archive.arm.gov.

References

Ackerman, T. P., and G. M. Stokes (2003), The atmospheric radiation measurement program, *Phys. Today*, *56*(1), 38–44.
Atlas, D., R. C. Srivastava, and R. S. Sekhon (1973), Doppler radar characteristics of precipitation at vertical incidence, *Rev. Geophys.*, *11*, 1–35.
Battaglia, A., C. D. Westbrook, S. Kneifel, P. Kollias, N. Humpage, U. Löhnert, J. Tyynelä, and G. W. Petty (2013), G-band (140–220 GHz) atmospheric radars: New frontiers in cloud physics, *Atmos. Meas. Tech.*, *7*, 1527–1546.
Beheng, K. D. (2010), The evolution of raindrop spectra: A review of microphysical essentials, in *Rainfall: State of the Science, Geophys. Monogr. Ser.*, edited by F. Y. Testik and M. Gebremichael, pp. 29–48, AGU, Washington, D. C.
Brown, P. S. (1993), Analysis and parameterization of the combined coalescence, breakup, and evaporation processes, *J. Atmos. Sci.*, *50*, 2940–2951.
Comstock, K. K., S. E. Yuter, R. Wood, and C. S. Bretherton (2007), The three-dimensional structure and kinematics of drizzling stratocumulus, *Mon. Weather Rev.*, *135*(11), 3767–3784.
Flynn, C., and C. Sivaraman (1998, updated hourly), Raman LIDAR Vertical Profiles (10RLPROFMR1TURN). 2011-09-14 to 2011-09-15. Southern Great Plains (SGP) Central Facility, Lamont, OK (C1), Atmospheric Radiation Measurement (ARM) Climate Research Facility Data Archive, USA, Oak Ridge, Tenn. [Available at https://doi.org/10.5439/1027254, Data set accessed on 2016-05-31.]
Frisch, A. S., C. W. Fairall, and J. B. Snider (1995), Measurement of stratus cloud and drizzle parameters in ASTEX with a K_α-band doppler radar and a microwave radiometer, *J. Atmos. Sci.*, *52*, 2788–2799.

Hogan, R. J., P. N. Francis, H. Flentje, A. J. Illingworth, M. Quante, and J. Pelon (2003), Characteristics of mixed-phase clouds: 1. Lidar, radar and aircraft observations from CLARE'98, *Q. J. R. Meteorol. Soc.*, *129*, 2089–2116.

Hogan, R. J., N. Gaussiat, and A. J. Illingworth (2005), Stratocumulus liquid water content from dual-wavelength radar, *J. Atmos. Oceanic Technol.*, *22*, 1207–1218.

Hu, Z., and R. Srivastava (1995), Evolution of raindrop-size distribution by coalescence, breakup and evaporation: Theory and observation, *J. Atmos. Sci.*, *52*, 1761–1783.

Kalesse, H., W. Szyrmer, S. Kneifel, P. Kollias, and E. Luke (2016), Fingerprints of a riming event on cloud radar Doppler spectra: Observations and modeling, *Atmos. Chem. Phys.*, *16*, 2997–3012.

Kruger, A., and W. F. Krajewski (2002), Two-dimensional video disdrometer: A description, *J. Atmos. Oceanic Technol.*, *19*, 602–617.

Kumjian, M. R., and O. P. Prat (2014), The impact of raindrop collisional processes on the polarimetric radar variables, *J. Atmos. Sci.*, *71*, 3052–3067.

Kumjian, M. R., and A. V. Ryzhkov (2010), The impact of evaporation on polarimetric characteristics of rain: Theoretical model and practical implications, *J. Appl. Meteorol. Climatol.*, *49*, 1247–1267.

Lebsock, M. D., K. Suzuki, L. F. Millán, and P. M. Kalmus (2015), The feasibility of water vapor sounding of the cloudy boundary layer using a differential absorption radar technique, *Atmos. Meas. Tech.*, *8*(9), 3631–3645.

Li, X., and R. C. Srivastava (2001), An analytical solution for raindrop evaporation and its application to radar rainfall measurements, *J. Appl. Meteorol.*, *40*, 1607–1616.

Marshall, J. S., and W. M. Palmer (1948), The distribution of raindrops with size, *J. Atmos. Sci.*, *5*, 165–166.

Mather, J. H., and J. W. Voyles (2013), The ARM climate research facility: A review of structure and capabilities, *Bull. Am. Meteorol. Soc.*, *94*, 377–392.

Matthews, A., B. Isom, D. Nelson, I. Lindenmaier, J. Hardin, K. Johnson, and N. Bharadwaj (2011a, updated hourly), Ka ARM Zenith Radar (KAZRSPECCMASKGECOPOL). 2011-09-15 to 2017-05-30. Southern Great Plains (SGP) Central Facility, Lamont, OK (C1). Atmospheric Radiation Measurement (ARM) Climate Research Facility Data Archive, Oak Ridge, Tenn. [Available at https://doi.org/10.5439/1025218], Data set accessed on 2016-05-31.

Matthews, A., B. Isom, D. Nelson, I. Lindenmaier, J. Hardin, K. Johnson, and N. Bharadwaj (2011b, updated hourly), W-band Scanning ARM Cloud Radar (WSACRSPECCMASKCOPOL). 2011-09-14 to 2011-09-15. Southern Great Plains (SGP) Central Facility, Lamont, OK (C1). Atmospheric Radiation Measurement (ARM) Climate, Oak Ridge, Tenn. [Available at https://doi.org/10.5439/1150288, Data set accessed on 2016-05-31.]

McFarquhar, M. G. (2004), The effect of raindrop clustering on collision-induced break-up of raindrops, *Q. J. R. Meteorol. Soc.*, *130*, 2169–2190.

O'Connor, E. J., R. J. Hogan, and A. J. Illingworth (2005), Retrieving stratocumulus drizzle parameters using doppler radar and lidar, *J. Appl. Meteorol.*, *44*, 14–27, doi:10.1175/JAM-2181.1.

Pruppacher, H. R., and J. D. Klett (1997), *Microphysics of Clouds and Precipitation*, Kluwer Acad., Dordrecht, Netherlands.

Rogers, R. R., and M. K. Yau (1989), *A Short Course in Cloud Physics*, 290 pp., Butterworth-Heinemann, Woburn, Mass.

Rosenfeld, D., and Y. Mintz (1988), Evaporation of rain falling from convective clouds as derived from radar measurements, *J. Appl. Meteorol.*, *27*, 209–215.

Seifert, A. (2008), On the parameterization of evaporation of raindrops as simulated by a one-dimensional rainshaft model, *J. Atmos. Sci.*, *65*(11), 3608–3619.

Srivastava, R. C. (1987), A model of intense downdrafts driven by the melting and evaporation of precipitation, *J. Atmos. Sci.*, *44*, 1752–1774.

Tridon, F., and A. Battaglia (2015), Dual-frequency radar Doppler spectral retrieval of rain drop size distributions and entangled dynamics variables, *J. Geophys. Res. Atmos.*, *120*, 5585–5601, doi:10.1002/2014JD023023.

Tridon, F., A. Battaglia, and P. Kollias (2013), Disentangling Mie and attenuation effects in rain using a K_a-W dual-wavelength Doppler spectral ratio technique, *Geophys. Res. Lett.*, *40*, 5548–5552, doi:10.1002/2013GL057454.

Tridon, F., A. Battaglia, E. Luke, and P. Kollias (2017), Rain retrieval from dual-frequency radar doppler spectra: Validation and potential for a midlatitude precipitating case study, *Q. J. R. Meteorol. Soc.*, *143*, 1364–1380, doi:10.1002/qj.3010.

Turner, D. D., R. A. Ferrare, L. A. H. Brasseur, W. F. Feltz, and T. P. Tooman (2002), Automated retrievals of water vapor and aerosol profiles from an operational Raman lidar, *J. Atmos. Oceanic Technol.*, *19*, 37–50.

Williams, C. R. (2016), Reflectivity and liquid water content vertical decomposition diagrams to diagnose vertical evolution of raindrop size distributions, *J. Atmos. Oceanic Technol.*, *33*, 579–595.

Worden, J., D. Noone, and K. Bowman (2007), Importance of rain evaporation and continental convection in the tropical water cycle, *Nature*, *445*, 528–532, doi:10.1038/nature05508.

Xie, X., R. Evaristo, S. Troemel, P. Saavedra, C. Simmer, and A. Ryzhkov (2016), Radar observation of evaporation and implications for quantitative precipitation and cooling rate estimation, *J. Atmos. Oceanic Technol.*, *33*, 1779–1792, doi:10.1175/JTECH-D-15-0244.1.